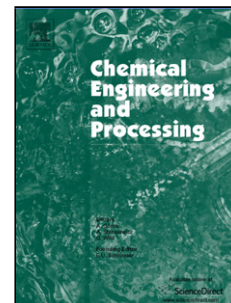


Journal Pre-proof

Metallic iron nanoparticles intensified production by Spinning Disk Reactor: optimization and fluid dynamics modelling

Giorgio Vilardi, Marco Stoller, Luca Di Palma, Kamelia Boodhoo, Nicola Verdone



PII: S0255-2701(19)30345-9

DOI: <https://doi.org/10.1016/j.cep.2019.107683>

Reference: CEP 107683

To appear in: *Chemical Engineering and Processing - Process Intensification*

Received Date: 26 March 2019

Revised Date: 10 August 2019

Accepted Date: 6 October 2019

Please cite this article as: Vilardi G, Stoller M, Di Palma L, Boodhoo K, Verdone N, Metallic iron nanoparticles intensified production by Spinning Disk Reactor: optimization and fluid dynamics modelling, *Chemical Engineering and Processing - Process Intensification* (2019), doi: <https://doi.org/10.1016/j.cep.2019.107683>

This is a PDF file of an article that has undergone enhancements after acceptance, such as the addition of a cover page and metadata, and formatting for readability, but it is not yet the definitive version of record. This version will undergo additional copyediting, typesetting and review before it is published in its final form, but we are providing this version to give early visibility of the article. Please note that, during the production process, errors may be discovered which could affect the content, and all legal disclaimers that apply to the journal pertain.

© 2019 Published by Elsevier.

Metallic iron nanoparticles intensified production by Spinning Disk Reactor: optimization and fluid dynamics modelling

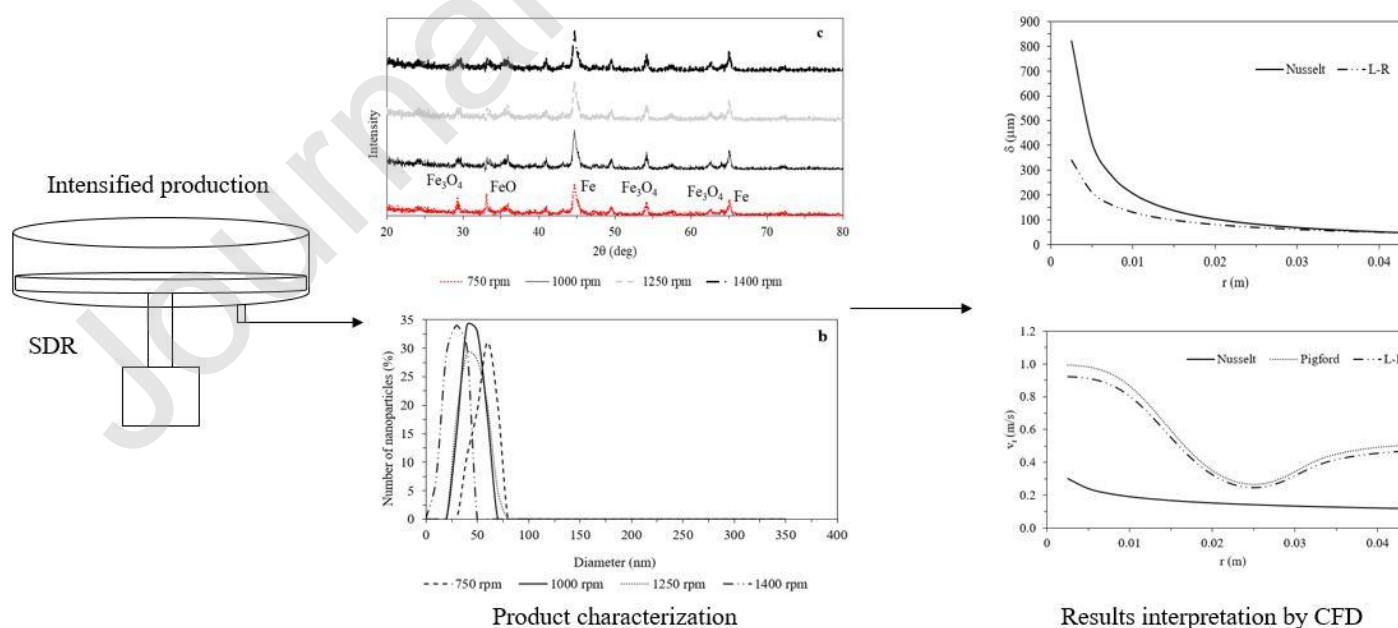
Giorgio Vilardi^{a*}, Marco Stoller^a, Luca Di Palma^a, Kamelia Boodhoo^b, Nicola Verdone^a

^a Sapienza University of Rome, Dept. of Chemical Engineering Materials Environment, Via Eudossiana 18,
00184, Rome, Italy

^b Chemical Engineering, School of Engineering, Merz Court, Newcastle University, Newcastle Upon Tyne, NE1
7RU, UK

*e-mail address: giorgio.vilardi@uniroma1.it, Tel +390644585580, Fax: +390644585451

Graphical Abstract



Highlights

- nZVI particles production has been successfully intensified by SDR technology
- The optimal operating parameter values allowed to obtain unimodal PSD
- The continuous production of nZVI was in the range 0.24-24 kg/d
- 2D and 3D models resulted necessary to avoid erroneous data interpretation

Abstract

The aim of this work was to investigate the optimization of iron nanoparticles production by spinning disk reactor. The influence of the two main operating parameters, i.e. rotational velocity and feed injection point position was investigated through evaluating the particle size distribution, the X-Ray powder diffraction spectra and metallic iron percentage production. Results showed that increasing both rotational velocity and the distance of reagents injection feed points from the disk centre led, to the production of metallic iron nanoparticles characterized by lower mean size. In particular, the optimal rotational velocity was found to be 1400 rpm whereas the optimal distance of injection feed point from disk centre was found to be 3.5 cm. According to these operating parameter values it was possible to obtain monodisperse nanoparticles, characterized by a mean size of 28 ± 2.1 nm and a production in the range 0.24-24 kg/day depending on the initial Fe(II) concentration. The results were then interpreted in light of three fluid dynamics models able to simulate the rotating thin liquid film on the surface of the spinning disk reactor. The applicability of Nusselt model was also investigated and discussed.

Keywords: *nZVI; SDR; micro-mixing; length-scale.*

1. Introduction

Metallic and organic nanoparticles are of great interest for the industry due to their applications in several fields [1,2]. Research on this topic seeks to develop many procedures to synthesize nanoparticles, mostly at lab scale, batch-wise and with low yield [3,4]. These procedures generally do not suit industrial needs of continuous, high capacity production and usually the product characteristics require targeting narrow particle size distributions and high quality, which is difficult to achieve by traditional equipment [5]. Process intensification techniques aim at minimizing plant size of continuous, high yield equipment capable to produce specific sized, high quality nanoparticles, combined with an increase in energy efficiency, safety and cost reduction [6–13]. In particular, iron metallic nanoparticles (nano zerovalent iron, nZVI) have been extensively studied due to the various industrial [14] and environmental applications [15] and due to the notable enhancement with respect to conventional technologies [16–26]. nZVI can be successfully produced by wet-chemistry method, using as a precursor iron sulphate or iron chloride and as a reducing agent sodium borohydride [27–31]. The use of Spinning Disk Reactor for the synthesis of metallic nanoparticles has been widely studied in the last two decades [32–34], due to the remarkable applicability and simple scale-up of this technology in this specific field [35]. Other nanoparticles, such as iron-oxide based one as magnetite, has already been synthesized with SDR, obtaining a very narrow and tuneable particle size distribution in the range 5-10 nm [36]. The SDR consists of a rotating disk with a jet of one, two or more liquid feeds impinging onto the top surface of the disk, creating a thin and highly sheared film due to the high centrifugal forces, leading to very rapid mixing and short residence time [37–39]. The

uniform and rapid micromixing environment generation on the rotating disk represents the main advantage offered by SDR in nanoparticles production by precipitation methodology. Micromixing conditions provide better control on formation and local distribution of supersaturation in the liquid film, influencing nanoparticles nucleation and crystal growth kinetics (which is a function of molecular diffusion phenomenon to the growing crystals) [40]. The analogy between plug-flow reactor (PFR) and SDR has been proposed by various authors: at high rotational velocity values (>1000 rpm), low viscosities (close to that of water) and high inlet flowrates, the bulk flow behaviour of SDR and PFR were proved to be very close [41,42]. The achievement of PFR flow conditions allows to high conversion rates and very good product quality (unimodal distribution size) to be obtained, reducing at the same time the residence time in the reactor maximizing the product yield [43]. In the production of metallic nanoparticles the reduction of residence time is fundamental, as well as reaching micromixing conditions [44]. Indeed, the imperfect crystallisation of particles or the crystals aggregations are mainly caused by non-uniform and slow mixing, since the crystal nucleation is influenced by the mixing at molecular scale, i.e. micromixing. Therefore, the achievement of micromixing conditions in the reactor vessel represents a fundamental goal to increase local supersaturation values and to favour crystal nucleation rather than crystal growth [45]. SDR technology has demonstrated its suitability for the production of well dispersed and unimodal nanoparticles [39,43,46,47] and for this reason it was selected for the optimization of nZVI production.

In this study, nZVI particles were successfully produced by a lab-scale SDR equipment, using the classical borohydride reduction method and fixing inlet flowrates according to a previous study [43]. The initial iron precursor and reducing agent concentration, as well as their molar ratio, were fixed according to the optimal values obtained in a previous work

performed in batchwise with Rushton equipped baffled stirred tank reactor [48]. nZVI production optimization was then carried out varying the feed streams position on the disk and the rotational velocity. The obtained data (X-Ray powder Diffraction spectra, Particle Size Distribution and metallic iron percent content) were then interpreted through the computational fluid dynamics modelling of the used SDR, according to Nusselt, Pigford and Lepehin and Riabchuk models.

2. Experimental

2.1. Materials and Equipment

All the reagents were purchased from Sigma-Aldrich (Milan) and were of analytical grade. The solutions were prepared with deionized water. In detail, the following reagents were used: NaBH_4 , $\text{FeSO}_4 \cdot 7\text{H}_2\text{O}$ and CMC (Carboxy-Methyl Cellulose, as dispersing agent) (20000 g/mol). The SDR used in this work was schematized in Figure 1: it was composed of a static external cylinder and an inner rotating disc of Teflon (8.5 cm in diameter), where reaction takes place. The feed streams temperature was kept constant at 25°C through a water bath. The two reagent solutions were injected at five different distances from the disk center, r_i (cm). The rotational velocity of the disk can be increased up to 1400 rpm and the intern diameter of feed stream lines was 3 mm.

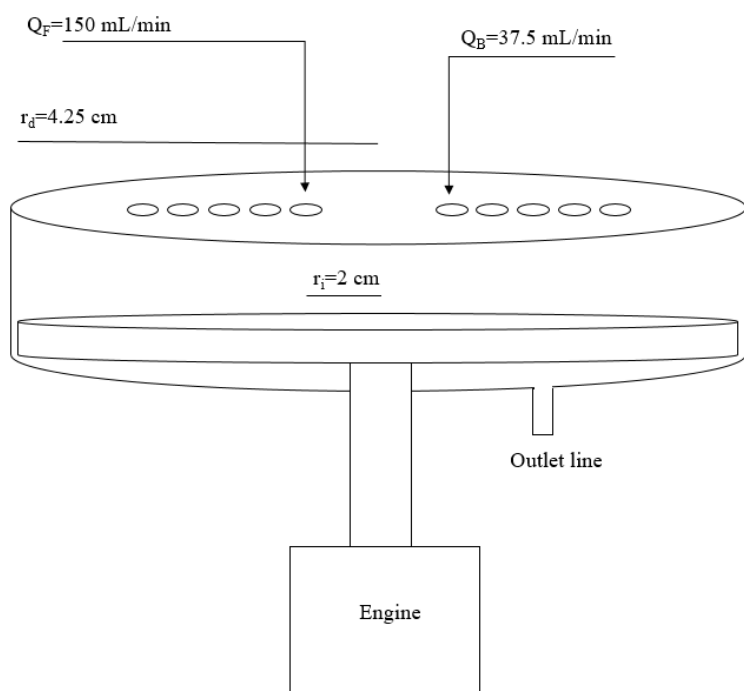


Figure 1: schematization of the SDR used in the experiments.

2.2. Analytical methods.

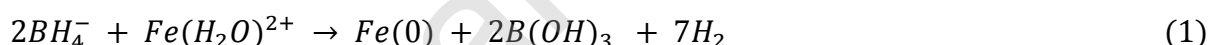
The PSD of the produced nanoparticles were characterized by Dynamic Light Scattering method, using a Zetasizer Nano ZS (Malvern). The Fe(0) (%) production was determined quantitatively by the titration method, based on the use of Fe(III) solution that oxidized the Fe(0), in an inert atmosphere of nitrogen to avoid Fe(0) oxidation due to oxygen corrosion, to soluble Fe(II) that can be determined by UV-Vis spectro-photometer at 565 nm using a derivative of triazine in thioglycolate medium. The method is reported in literature [49]. The Fe(0) (%) production was determined also qualitatively using X-Ray powder Diffraction (XRD) method, using a Bruker D8 Advance. The magnetophoretic collection of synthesized nanoparticles was tested using a N50 grade NdFeB cylindrical permanent magnet (radius of 0.025 m, thickness of 0.012 m and residual induction, B_r , of 1.45 T).

The solution viscosity has been measured in a previous work, according to the optimal CMC, NaBH_4 and $\text{FeSO}_4 \cdot 7\text{H}_2\text{O}$ concentrations and was equal to 2.2 mPas at 25°C [48]. The

synthesis was carried out using reagent solutions prepared with deionized water previously de-oxygenated for 4 hours at 50°C under nitrogen atmosphere. The nZVI were produced in open atmosphere, without using nitrogen, since the residence time in the reactor vessel was lower than 1 s and the possible oxidation of freshly prepared nanoparticles was considered negligible, as reported in next paragraphs.

2.3. Experimental procedure

The nZVI synthesis was performed according to a previous study [43] fixing the iron precursor flowrate, Q_F , to 150 mL/min and the reducing agent flowrate, Q_B , to 37.5 mL/min. The concentration of Fe salt was set to 0.02 M, according to a previous study [48] and considering the optimal $BH_4^-/Fe(II)$ mol/mol ratio equal to 3 and the fixed Q_F and Q_B values, the concentration of reducing agent was set equal to 0.24 M. The two inlet streams were placed symmetrically with respect to the disk centre [50]. In the first experimental runs the r_i was fixed equal to 2 cm [50] and selected rotational velocities, ω (rad/s or rpm), were tested: 78.54 (750 rpm), 104.72 (1000 rpm), 130.9 (1250 rpm) and 146.6 (1400 rpm) rad/s. The nZVI nanoparticles synthesis occurred according to the following reaction [48]:



The black solid particles appeared instantaneously to the addition of the reducing agent. The produced nanoparticles were collected, immediately characterized through the titration method and by Zetasizer whereas 10 mL of solution were vacuum filtered, dried and stored under nitrogen atmosphere for subsequent XRD analysis. The second series of experimental runs was performed fixing the ω to the optimal value found in the previous experiments and the influence of feed point-disk centre distance on the mean size of the produced nZVI was investigated, varying the r_i according to the following values for both inlet streams: 1.5, 2,

2.5, 3 and 3.5 cm. The produced nanoparticles were then characterized in terms of mean hydrodynamic diameter, d_m (nm), measured through the Zetasizer instrument. The Scanning Electron Microscope (SEM, JEOL Ltd.) was used to analyse the nanoparticles produced adopting the optimal operating parameter's values (see Supplementary Materials).

Each test was conducted in duplicate and the mean values were reported (the standard deviation in all tests was <3.7%).

2.4. Data interpretation and computational fluid dynamics simulations

The obtained PSD and d_m values were interpreted according to CFD simulations of the rotating liquid film generated on the top surface of the disk. The flow regime can be predicted basing on the Reynolds rotational number defined as follows [51]:

$$Re = \frac{\omega r^2}{\nu} \quad (2)$$

where ω (in this equation expressed in 1/s, in the following it will be reported as rpm or rad/s) is the rotational velocity of the disk, ν (m²/s) is the fluid kinematic viscosity and r (m) is the radius at the measurement point on the disc. The flow on the rotating disk can be classified as laminar, transitional or turbulent according to Re number values over the disk. In detail, according to a number of experiments reported in [51], the flow on a free rotating disk can be considered laminar for Re numbers lower than 10^4 , since in the range 10^4 - 10^5 the flow instabilities become significant and the flow can be considered in transition to turbulent conditions, fully established for Re number larger than 10^5 .

The rate of mixing, heat and mass transfer in the fluid is affected by the type of flow prevailing on a rotating disc surface under given conditions of flowrate and rotational speed. The fluid dynamics of a rotating liquid film can be described by the classical Navier-Stokes

equations in cylindrical coordinates (r, θ, z) obtaining a very complex differential equations system. Thus, several researchers [52–56] proposed various hypothesis to develop simple models to describe the hydrodynamic of rotating thin liquid film, as reported in the following paragraphs.

2.4.1 The centrifugal model

The simplest model to describe the flow on a rotating disk assumes that the liquid rotates at the same speed as the disc, so they are completely synchronized. Under these conditions, the centrifugal acceleration that drives the liquid film through the surface of the disk at the radius r can easily be estimated as $r\omega^2$. With this assumption, the flow over the disk can be considered analogous to that on a sloping surface. Nusselt elaborated this model while studying the fluid-dynamic behavior of a liquid film condensing. Nusselt considered it as a laminar flow on a sloping plane.

This assumption implies that the liquid has reached full flow conditions developed in which the weight of the film is perfectly balanced by the shear viscous forces. So, the model considers the Navier-Stokes equations and that of continuity in a cylindrical coordinate system and makes the following assumptions [35]:

- steady-state conditions;
- large rotational velocity, thus the system can be considered symmetric with respect to angular direction;
- uniform pressure;
- gravity force negligible influence on momentum transfer;
- negligible inertial forces and superficial instabilities ;

- thin liquid film thickness (δ (m)) lower than disk radius;
- laminar flow;
- Newtonian liquid;
- liquid velocity instantaneously reaches disk velocity and no tangential sliding occurs;
- liquid motion is radial on disk surface, thus Coriolis acceleration is neglected;
- T (K), v (m/s) and c (mmol/L) gradients are negligible if compared with those orthogonal to the disk surface.

Basing on these assumptions, the Navier-Stokes equation can be written as follows:

$$\begin{cases} -\frac{v_\theta^2}{r} - \nu \frac{\partial^2 v_r}{\partial z^2} = 0 \\ v_r \frac{\partial v_\theta}{\partial r} + \frac{v_r v_\theta}{r} - \nu \frac{\partial^2 v_\theta}{\partial z^2} = 0 \end{cases} \quad (3)$$

Since the radial component of the velocity, v_r (m/s) is lower than the tangential one, v_θ (m/s) and considering the ω of the liquid equal to that of the disk for each value of the distance from the center of rotation we can put $v_\theta = r\omega$ reducing the system previous to a single differential equation:

$$-r\omega^2 = \nu \frac{\partial^2 v_r}{\partial z^2} \quad (4)$$

The integration of eq. 4 can be performed considering for $z=0$ $v_r=0$ and $z=\delta$ $dv_r/dz=0$:

$$v_r(r, z) = \frac{r\omega^2}{\nu} \left(\delta z - \frac{z^2}{2} \right) \quad (5)$$

Starting from v_r the fully synchronized flow model can be used to obtain a reasonable estimate for a wide range of measures that characterize the flow on an SDR. Integrating from 0 to δ the average velocity can be obtained:

$$\bar{v}_r = \frac{1}{\delta} \int_0^\delta v_r(r, z) dz = \frac{r\omega^2 \delta^2}{3v} \quad (6)$$

And the inlet flow-rate can be expressed as:

$$Q = 2\pi r \delta \bar{v}_r \quad (7)$$

The Nusselt model assumes that the flow on a rotating disk is similar to that laminar of a liquid film flowing on a vertical wall, so the equations obtained here can also be easily derived substituting in the equations for the vertical wall, the gravitational constant g with $r\omega^2$. Nusselt showed that for a Newtonian fluid of kinematic viscosity ν , the thickness of the film δ , can be expressed in terms of the flow rate of liquid Q which falls on a inclined plane of width w under gravitational acceleration g using the following equation:

$$\delta = \left(\frac{3\nu Q}{wg} \right)^{1/3} \quad (8)$$

That for the disk can be written as:

$$\delta = \left(\frac{3\nu Q}{2\pi r^2 \omega^2} \right)^{1/3} \quad (9)$$

Eq. 9 can be substituted in Eqs. 5 and 6:

$$v_r(r, z) = \frac{r\omega^2}{v} \left(\frac{0.909 \frac{Q}{\pi \nu 2r}}{\left(\frac{r\omega^2}{v^2} \right)^{1/3}} z - \frac{z^2}{2} \right) \quad (10)$$

$$\bar{v}_r = \frac{r\omega^2}{3v} \frac{0.909 \frac{Q}{\pi \nu 2r}}{\left(\frac{r\omega^2}{v^2} \right)^{2/3}} \quad (11)$$

However, contrary to the analogous case of the film that runs along a vertical wall, in this case the steady state assumption does not subsist since the film thickness and radial velocity change continuously as flow flows along the disk. Thus, the average residence time on the

disk, τ (s), for a given feed radius, r_i , can be calculated considering that the average time needed to cover a portion dr is equal to $\bar{v}_r dt$. Therefore integrating the equation $\tau = \int_{r_i}^{r_d} (dr / \bar{v}_r)$ according to the conditions $t=0$ for $r=r_i$ and $t=\tau$ for $r=r_d$, one can obtain:

$$\tau = \left(\frac{81\pi^2 \nu}{16\omega^2 Q^2} \right)^{1/3} (r_d^{4/3} - r_i^{4/3}) \quad (12)$$

The average residence time and the thickness of the film are the two most important parameters of this model that most affect the transfer rate of energy and matter, as well as the rate of mixing and the effectiveness of the reactions occurred on the surface of the disk. From the previous equations it is possible to note that these two variables are controlled by the rotational velocity ω . A decrease of residence times and thickness film correspond to an increase of ω improving mixing and transfer of matter and heat. Therefore, the critical parameter to optimize to get the best operational performance of the SDR is just ω . The Nusselt's model is the simplest formulation of the Navier-Stokes equations and its validity is strongly bounded by the assumptions on which it is based. Various experimental studies have shown that the film thickness is lower than the predicted one from Nusselt, especially due to the effect of surface waves on the flow through the disk [57].

The integration of the film thickness and velocity equation can be used to calculate other "global" measures of the flow conditions on the disk. For instance, by integrating the expression of the film thickness one can obtain the measurement of the volume of liquid (m^3) on the surface of the disc:

$$V = \left(\frac{81\pi^2 \nu Q}{16\omega^2} \right)^{1/3} r_d^{4/3} \quad (13)$$

Other useful global measures are reported below:

$$\delta^m = \frac{v}{\pi r_{disk}^2} \approx 1.17 \left(\frac{vQ}{r_d^2 \omega^2} \right)^{\frac{1}{3}} \quad (14)$$

$$v_r^m = \frac{Q r_{disk}}{V} \approx 0.27 \left(\frac{Q^2 \omega^2}{v r_d} \right)^{\frac{1}{3}} \quad (15)$$

2.4.2 The Pigford model

Nusselt model is considered a very simple model and can not be used when the rotational velocity is large or, in general in full turbulent flow. Burns and co-authors [58] have demonstrated that Nusselt model can not be used when the Ekman number is lower than 2 ($E=v/\delta^2\omega$). The number of Ekman is defined as the ratio between the inertial and viscous contributions referred to the flow of a fluid on the spinning disc. Usually E dimensionless number value can be calculate to evaluate if a flow has reached the rotational synchronized conditions. Inertial contributions are very significant for lower Ekman numbers and the thickness of the measured film deviates noticeably from the predicted Nusselt values in these cases. Indeed, when $E<2$, the inertial contributions have a considerable contribution and a more complex two-dimensional model is required. A two-dimensional model for fluid flows over a rotating disk that takes into account both inertial and viscous contributions, was developed by Wood and Watts [56], i.e. the Pigford model. Burns gave a comparison of this model outputs with experimental data. Pigford model can be written in terms of radial and tangential velocity and consists of the following equations:

$$\begin{cases} v_r \frac{\partial v_r}{\partial r} - \frac{v_\theta^2}{r} + \frac{12v_r^3 K_1 r^2 \pi^2 v}{Q^2} = 0 \\ v_r \frac{\partial v_\theta}{\partial r} + \frac{v_r v_\theta}{r} - \frac{12v_r^2 K_2 r^2 \pi^2 v}{Q^2} (r\omega - v_\theta) = 0 \end{cases} \quad (16)$$

Where K_1 (usually in the range 0.5-0.7 and set equal to 0.61 according to experimental data fitting of Burns) and K_2 (equal to λ_E/λ_{E0} , where λ_E is a length scale beyond that inertial and viscous forces have the same magnitude order and $\lambda_{E0}= 10.8$ cm) are empirical corrective constants for viscous terms:

$$\lambda_E = \left(\frac{Q^2}{\omega v}\right)^{1/4} \quad (17)$$

The boundary conditions are $-v_r=4Q/\pi d^2$ and $v_\theta=0$ for $r=d/2$, where d (mm) is the diameter of the feed flow distributor.

2.4.3 Lepehin and Riabchuk model

A more reliable model, if compared with the previous ones, is the Lepehin and Riabchuk (L-R) 3D model, based on the assumptions of: (i) axial-symmetric laminar flow, (ii) inertial forces negligible with respect to Coriolis and centrifugal ones and (iii) constant pressure in the liquid film (equal to the atmospheric value). The model can be expressed according to the following two equations [59,60]:

$$\begin{cases} v \frac{\partial^2 v_r}{\partial z^2} - 2\omega v_\theta = \omega^2 r \\ v \frac{\partial^2 v_\theta}{\partial z^2} + 2\omega v_r = 0 \end{cases} \quad (18)$$

Coupling this system with the integral form of continuity equation:

$$Q = 2\pi r \int_0^\delta v_r dz \quad (19)$$

and solving the new system with the proper initial and boundary conditions [60], the following equation is obtained:

$$\delta = 0.886 Q^{0.348} v^{0.328} \omega^{-0.676} r^{-0.7} \quad (20)$$

The above mentioned models were implemented in gPROMS environment (ver. 4.0) and the software was used to simulate the hydrodynamics of the SDR according to the fixed operating conditions. Finally, the mixing intensity can be estimated through the obtained specific power dispersed on the rotating disk, ε (W/kg), values. According to [37] ε can be expressed as follows:

$$\varepsilon = \frac{1}{2\tau} \left[(\omega^2 r^2 + \bar{v}_r^2)_{out} - (\omega^2 r^2 + \bar{v}_r^2)_{feed} \right] \quad (21)$$

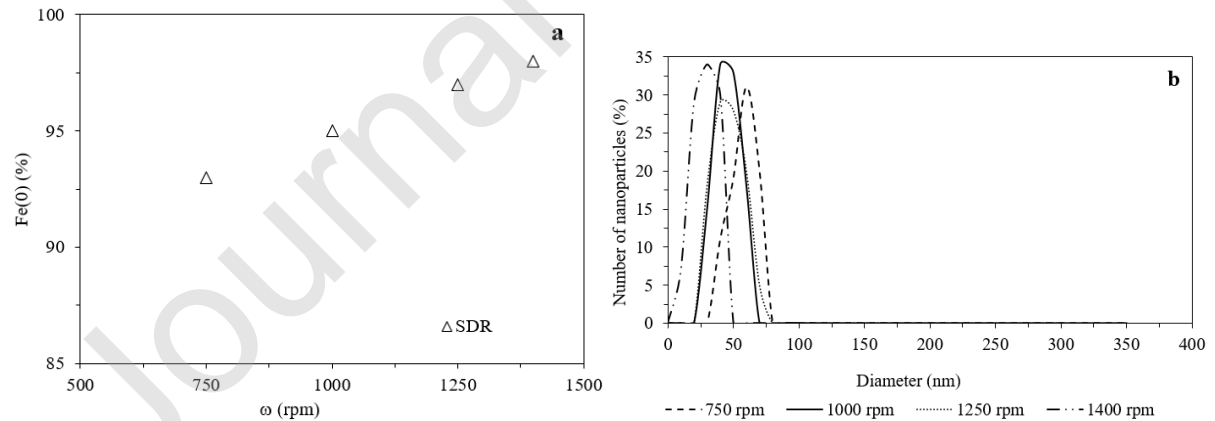
Whereas the mixing time can be calculated as [47]:

$$\tau_{mix} = 12 \left(\frac{\nu}{\varepsilon} \right)^{0.5} \quad (22)$$

3. Results and discussion

3.1 nZVI production: the influence of rotational velocity

Figure 2 shows the results of characterization of the nZVI produced varying the rotational velocity of the disk.



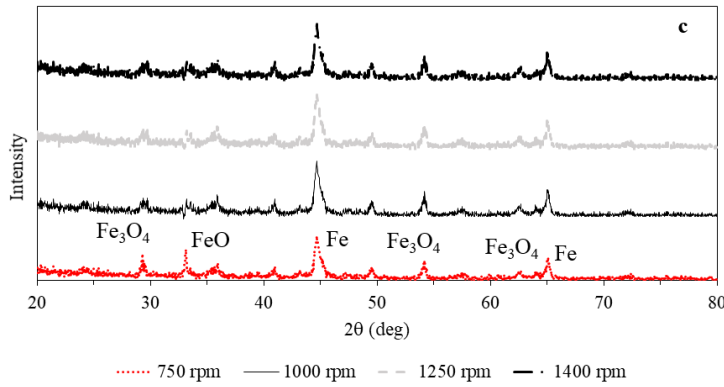


Figure 2. Fe(0) (%) production (a), PSD (b) and XRD (c) of nZVI produced at different ω ($Q_F=150$ mL/min, $Q_B=37.5$ mL/min, $T=25^\circ\text{C}$).

The Fe(0) (%) content increases with the rotational velocity increase, since the conversion of Fe(II) resulted favoured by an increase of ε and Re (see Table 1), that also determines an increase of Sh (Sherwood number is a function of Re and Schmidt number, Sc , where $Sh=k_m L/D$ and $Sc=\nu/D$, with k_m (m/s) the mass transfer coefficient, D (m^2/s) the diffusion coefficient of the Fe(II) ions, and L (m) is the characteristic length that in this case should be equal to δ) and thus of the mass transfer rate [52,61].

Table 1

Calculated parameters of the first runs (Nusselt).

		ω (rpm)			
Parameter	Unit	750	1000	1250	1400
δ^m	m	9.9E-05	8.2E-05	7.1E-05	6.5E-05
v_r^m	m/s	0.23	0.28	0.33	0.35
τ	s	0.114	0.094	0.081	0.076
V	mL	0.564	0.466	0.401	0.372
ε	W/kg	37.88	81.58	147.91	200.11
τ_{mix}	s	0.0029	0.0020	0.0015	0.0013

As expected, the best performances were achieved at the maximum rotational velocity of 1400 rpm, since the Fe(0)(%) was 98.3%, the mean size of the nanoparticles was 28 ± 2.1 nm and the peaks of iron oxide species were negligible in the XRD spectrum. In particular, the SDR allowed to obtain always an unimodal distribution size of the produced nanoparticles rather than a bimodal one, as obtained for some ω values by means of Rushton equipped baffled stirred tank reactor [48]. The XRD spectra clearly show the presence of the typical peak at 45° of α -iron [62]. Indeed, the characteristic peaks of iron oxide crystalline phases (close to 63°) are also present, indicating that the particles were partially oxidized during the preparation of the sample. As reported by various authors, the presence of iron oxides as thin layer is necessary to prevent further oxidation of the product before its use [63–68]. The typical peaks of FeO and magnetite were well evident in the sample from the first runs at 750 rpm, whereas they tended to disappear with the rotational velocity increase, since the Fe(II) conversion rose, as reported in Figure 1a. Through the application of the Scherrer equation [69] an average crystal's size of 24 nm has been derived, that was lower than the mean dimension measured by DLS. This can be explained considering that the DLS measurement tend to slightly overestimate the particle's dimension, since this method measures the hydrodynamic diameter. In addition, the SEM photo (see Supplementary Materials) clearly showed that the particle's dimension varied in the range 20–40 nm. The obtained nanoparticles were characterized by a lower mean dimension with respect to those reported in a previous work, as visible in the HRTEM also reported [70] (in that case the particles were produced in batch systems without the use of any dispersing agent, showing a typical core-shell structure as reported in various studies [62,71]). The magnetophoretic separation of the produced nanoparticles has been tested by means of a permanent magnet. The actual

magnetic field of the permanent magnet, B_x (T), along its symmetric axis, has been calculated according to the following equation [72]:

$$B_x = \frac{B_r}{2} \left[\frac{x + L}{\sqrt{(L + x)^2 + R^2}} - \frac{x}{\sqrt{x^2 + R^2}} \right] \quad (23)$$

where B_r (T) is the residual induction, x is the distance from the magnet face in contact with the becker bottom, R (m) is the magnet radius and L (m) its thickness. Figure S3 displays the B_x variation along the symmetric x axis. The B_x decreased from 0.31 up to 0.043 from the bottom to the top of the liquid (0.038 m). The complete nanoparticle separation occurred after 8 min (see Supplementary Materials). Analogous results have been reported for other iron-based nanoparticles in literature [73–75].

The micro-mixing time of the last runs ($\omega=1400$ rpm) was significantly lower in comparison to that of the first runs ($\omega=750$ rpm) and this improved the performance of the nZVI production process, since for very fast reaction as the one studied in this work, a large mixing efficiency is fundamental to achieve homogeneous and high quality product [41,54,76]. Furthermore, only for $\omega=1400$ rpm the mixing time reached the order of magnitude of 1 ms, that represents the typical value for the attainment of micromixing conditions [37].

Analogous considerations can be drawn considering the ε values, that increased from 37.88 W/kg up to 200.11 W/kg passing from $\omega=750$ rpm to $\omega=1400$ rpm, implying a remarkable improvement in the dissipated energy in the reaction volume. Other important considerations can be made based on the values of δ^m , V , v^m and τ . The average film thickness and reaction volume are correlated, and a ω value increase led to a reduction of these parameters, leading to an enhancement of mass transfer rate during the reaction. This was mainly due to the characteristic length decrease of the phenomenon, i.e. the δ , causing, at the same time, an increase of the mass transfer coefficient at fixed hydrodynamic and liquid physical

conditions. Regarding the latter two parameters, an increase of average liquid radial velocity caused a decrease of the residence time, enhancing the convective mass transfer rate and, therefore, the reaction performances.

In terms of the hydrodynamics of the thin rotating film, Figure 3 displays the Re values variation along the r_m at the maximum ω value.

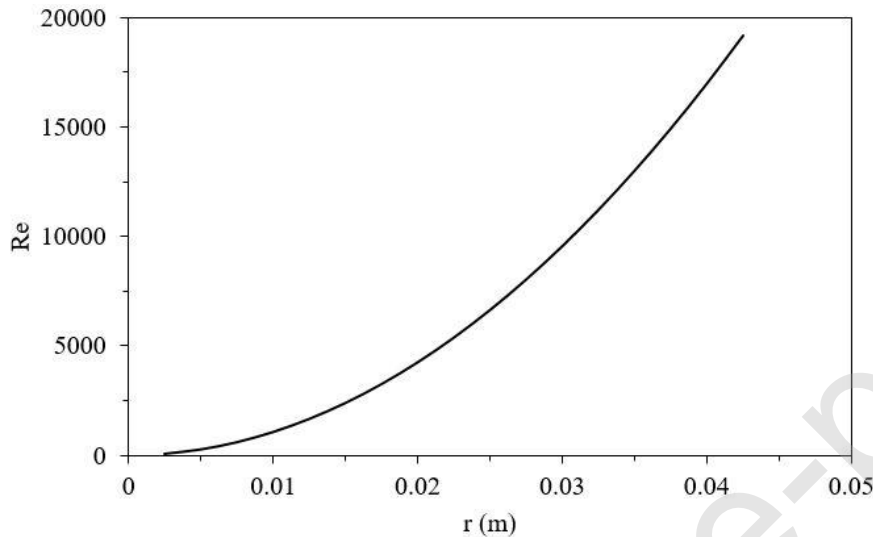


Figure 3: Re values varying the radial distance on the disk ($\omega=1400$ rpm).

The Reynolds number rapidly increased from the centre of the disk to the edge, achieving a maximum value of about 1.92×10^4 , indicating that the flow was mainly laminar up to $r=0.03$ m (where Re was equal to 0.95×10^4) and then displayed transitional flow characteristics across the rest of the disc surface to the periphery characteristics across the rest of the disc surface to the periphery, without reaching turbulent conditions. However, this result alone can not justify the use of Nusselt model to describe the thin film hydrodynamics, since the Ekman number should be considered. In particular, the calculated E number was 2.81, 3.1, 3.33 and 3.46 according to increasing ω values, implying that the prediction made by Nusselt model could be considered a first approximation, that usually tends to return v_r values lower

in comparison with those experimentally measured [58,77]. Indeed, the E number was calculated using the δ^m , but, as it is well known, the δ varies along the radial coordinate over the disk surface, implying that local E numbers should be considered due to the variation of E in the rotating domain. For this reason, in the following paragraph, two other models were considered for the interpretation of the results from the second series of experiments and the description of the established hydrodynamic fields; it will be clear that Nusselt predictions were not accurate even if $E > 2$.

Finally, the optimal rotational velocity value was found to be 1400 rpm and this value was fixed for the subsequent runs.

3.2 The influence of injection feed point on the nZVI mean size and CFD modelling

Figure 4 displays d_m trend with the r_i variation.

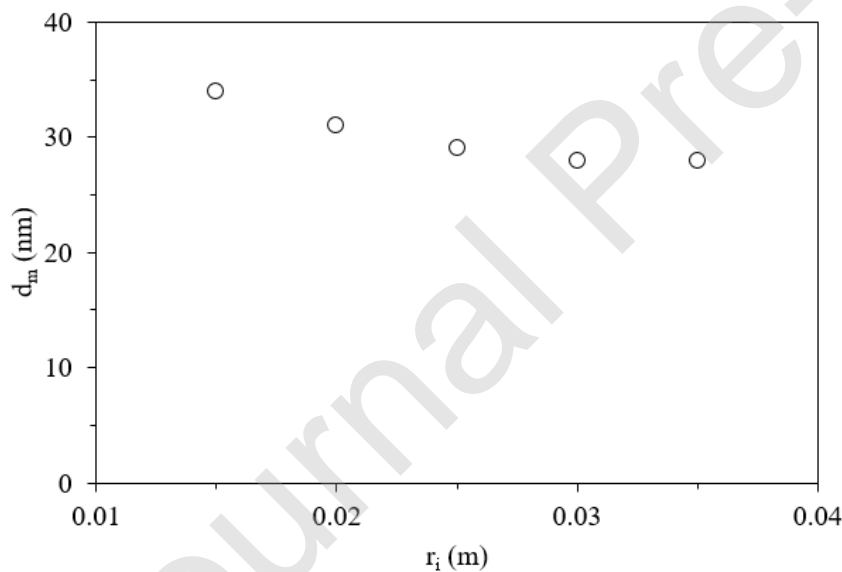


Figure 4: nZVI mean size produced at different r_i values ($T=25^\circ\text{C}$, $\omega=1400$ rpm, $Q_F=150$ mL/min, $Q_B=37.5$ mL/min).

All the PSDs were unimodal (data not reported) and the optimal r_i value was found to be 0.035 m, since the obtained d_m for these runs was the minimum value, i.e. 28 ± 2.1 nm. The trend between r_i and mean nZVI size was found to be inversely proportional. Indeed, the variation of r_i strongly influences the specific energy power dispersed on the rotating disk, since it appears in both eqs. 11, 12 and 21. Furthermore, the ε value can be calculated considering the different mean radial velocity predictions made by the specific employed fluid dynamic model, yielding different ε values (Table 2).

Table 2

Calculated parameters of the second runs according to the three models.

r_i (m)	Parameter	Unit	Model		
			Nusselt	Pigford	L-R
0.015	τ	s	0.089		
	ε	W/kg	190.03	189.04	189.67
0.020	τ	s	0.076		
	ε	W/kg	200.04	199.36	199.65
0.025	τ	s	0.060		
	ε	W/kg	210.15	209.55	209.78
0.030	τ	s	0.044		
	ε	W/kg	220.10	219.605	219.797
0.035	τ	s	0.027		
	ε	W/kg	229.94	229.52	229.68

The ε value increased with an increase of r_i (as reported in eq.(12) an increase of r_i causes a significant decrease of residence time on the disk and the ε is inversely proportional to τ) and this trend might explain the decreasing nZVI mean size trend. In fact, at higher ε values it was expected to obtain nanoparticles characterized by lower mean size, since the micromixing efficiency resulted maximized since the mixing time decreased. Analogous results were reported by other authors on the same SDR equipment, obtaining lower

nanohydroxyapatite mean sizes for higher ε and r_i values [47]. Another important result was that the differences among ε values predicted using radial velocity values from the three employed models were negligible, notwithstanding the remarkable differences of the predicted hydrodynamic fields, as reported in Table 3 and Figures 5 and 6. However, as it will be showed in the following, after a deeper discussion about the ε calculation procedure, the apparent negligible differences among ε values will be considerable.

Table 3

Calculated average radial velocities according to the three models.

		Model		
		Nusselt	Pigford	L-R
r_i (m)	v_r (m/s)			
0.015	feed	0.166	0.581	0.414
	out	0.117	0.383	0.306
0.020	feed	0.182	0.518	0.414
	out	0.117	0.383	0.306
0.025	feed	0.140	0.474	0.379
	out	0.117	0.383	0.306
0.030	feed	0.131	0.440	0.352
	out	0.117	0.383	0.306
0.035	feed	0.125	0.414	0.331
	out	0.117	0.383	0.306

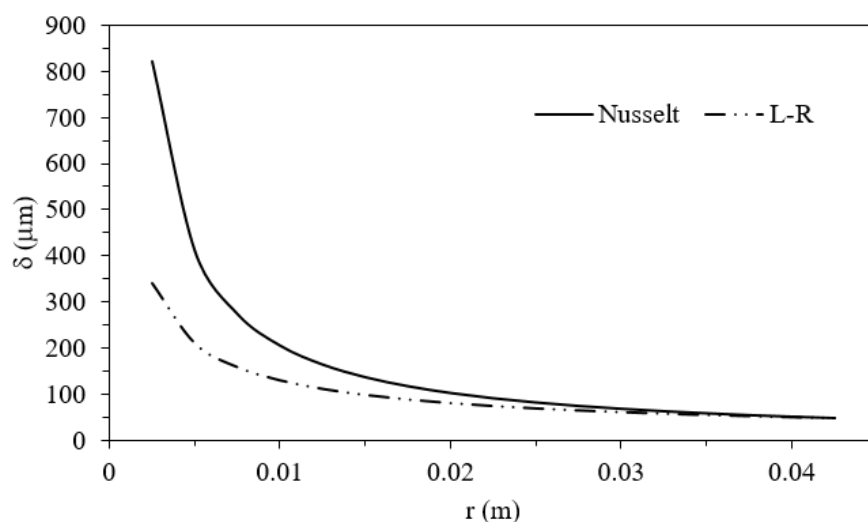


Figure 5: film thickness values at different r , according to the three different fluid dynamic models ($T=25^{\circ}\text{C}$, $\omega=1400$ rpm, $Q_F=150$ mL/min, $Q_B=37.5$ mL/min).

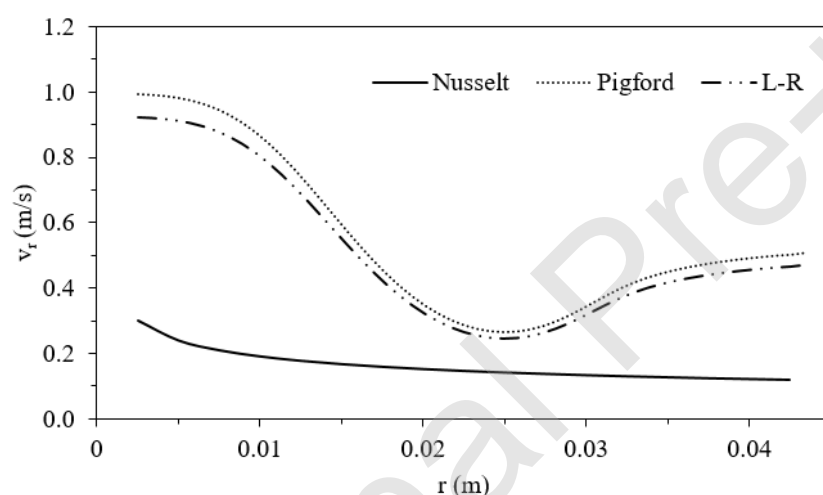


Figure 6: average radial velocity values at different r , according to the three different fluid dynamic models ($T=25^{\circ}\text{C}$, $\omega=1400$ rpm, $Q_F=150$ mL/min, $Q_B=37.5$ mL/min).

The δ values predicted by Nusselt model were always larger in comparison with those predicted by L-R one. On the contrary, the v_r values predicted by Nusselt model were always lower than those predicted by the latter ones. The Nusselt model was not able to predict the

spin-up zone, i.e. the zone after that the liquid is rotating close to the disk velocity and results synchronized with it. In Figure 6 the spin-up zone is well visible for v_r trends predicted by Pigford and L-R models. According to Burns and co-authors, the distance from the disk centre with respect the spin-up zone appears, r_s (m), can be calculated by the following equation [58,77]:

$$r_s = 0.88\lambda_E \left(\frac{d}{2\lambda_E} \right)^{-0.025} K_1^{0.11} K_2^{-0.37} \quad (24)$$

This yields a value of 0.0267 m that is in agreement with the local minimum observed in Figure 6 for both Pigford and L-R v_r trends.

Another important consideration should be made about the E number. Considering that the film thickness varies with the radial distance over the disk surface, also the E number will undergo to a substantial variation, since it is inversely proportional to δ^2 (Figure 7).

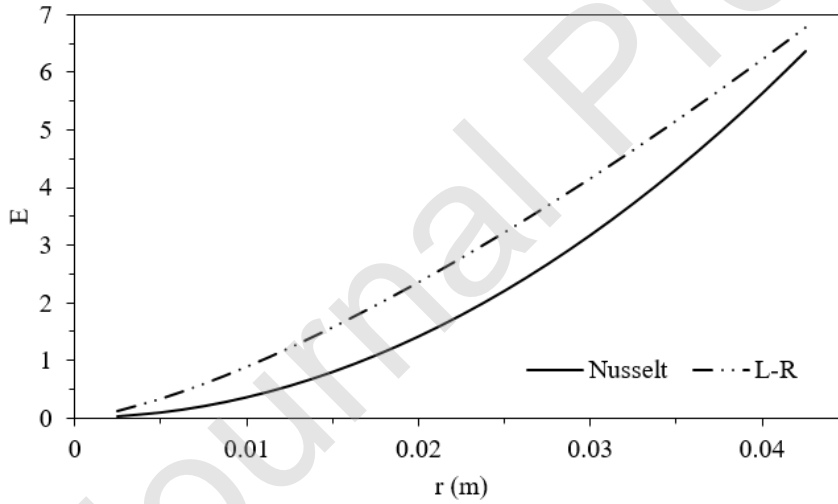


Figure 7: Ekman number values at different r_i (i.e. δ) ($T=25^\circ\text{C}$, $\omega=1400$ rpm, $Q_F=150$ mL/min, $Q_B=37.5$ mL/min).

As reported by Figure 7, the E number was always lower than 2 up to $r_i=0.025$ and 0.0175 m according to Nusselt and L-R models, respectively. This means that inertial forces are very important along the radial distance that includes about an half of the studied rotating film surface, implying that more accurate models than Nusselt one, such as Pigford and L-R models, should be used to well describe the hydrodynamic field. However, as demonstrated by the very close calculated ε values according to the three models, the notable difference observed for the hydrodynamic field's related parameter was not observed for the specific energy power dispersed on the rotating disk. The more probable explanation could be that the average residence time that appears in eq. 21 should be substituted with another expression that takes into account the radial velocity. Therefore, a different equation should be used to calculate the residence time, as reported below:

$$t_{res} = \frac{2(r_d - r_i)}{\bar{v}_{rout} + \bar{v}_{rfeed}} \quad (25)$$

Table 4 reports the ε and t_{res} calculated according the v_r predicted by the three fluid dynamic models.

Table 4

ε and t_{res} according to the three fluid dynamic models.

r_i (m)	Parameter	Unit	Model		
			Nusselt	Pigford	L-R
0.015	t_{res}	s	0.195	0.057	0.076
	ε	W/kg	87.24	296.23	222.20
0.020	t_{res}	s	0.150	0.050	0.062
	ε	W/kg	100.39	301.37	241.45
0.025	t_{res}	s	0.136	0.041	0.051
	ε	W/kg	93.03	309.81	248.12
0.030	t_{res}	s	0.101	0.030	0.038
	ε	W/kg	96.72	320.02	256.24

0.035	t_{res}	s	0.062	0.019	0.024
	ε	W/kg	100.66	331.30	265.23

As clearly showed in Table 4, Nusselt model overestimates the residence time values, i.e. underestimates the radial velocity values, as already observed by Burns and co-workers [58,77]. This implies that the calculated ε values through t_{res} estimated by Nusselt's v_r values resulted in notably lower values than those reported for Pigford and L-R models that, conversely, were of the same order of magnitude.

The reported results are quite important since they showed that, even if the E number values were larger than 2 in a wide part of the rotating domain according to L-R model, the Nusselt model's predictions, in terms of both hydrodynamic field and energy-related parameters, were not in agreement with those obtained by more complex models. Moreover, besides the considerations made on E values, it is necessary to underline that the predictions made by Nusselt model may significantly vary from those made through 2D or 3D models, Pigford and L-R models respectively, even if the overall flow regime on the rotating disk can be considered laminar. In conclusion, 2D and 3D models should be in any case preferred rather than 1D model to avoid notable errors in the interpretation of the results obtained by SDR experimentations.

Finally, Figure 8 displays the power relation between the obtained d_m and the calculated ε according to the three fluid dynamic models for all the performed runs, using the eq. 24 for the residence time calculation.

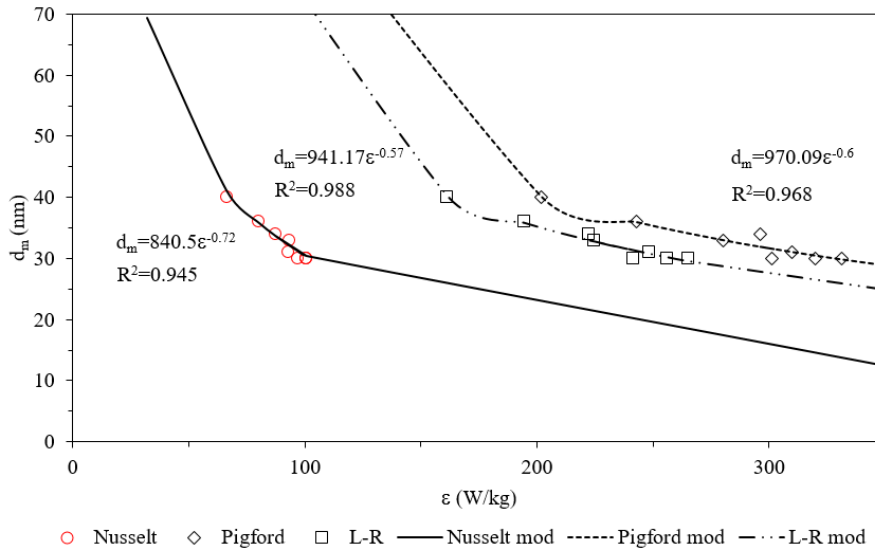


Figure 8: correlation between nZVI mean size and ϵ calculated by Nusselt (a), Pigford (b) and L-R (c) models.

It is important to underline that the exponent of ϵ obtained by the fitting of L-R model was closer to -0.5, that is the dependence both of micromixing and mesomixing times with respect to ϵ [78]. The obtained trends well describes the relation between nZVI mean size and specific energy power dispersion, as previously discussed and demonstrated in a previous work [47]. Therefore, to obtain a lower mean size of the produce nanoparticles it can be useful increasing both rotational velocity and the distance between injection feed points and disk centre. However, to support again the discussion about the necessity to use more reliable model with respect to Nusselt one, the best fit between d_m and ϵ data was obtained for L-R, followed by Pigford model.

Finally, the nZVI production per day, P (kg/day) was calculated using the following equation:

$$P = Q_F * 60 * 24 * [Fe(II)]_0 * Fe(0)(\%) * \frac{M_{Fe}}{1000} \quad (26)$$

where Q_F is in L/min and M_{Fe} (55.84 g/mol) is the iron molar mass. A P value in the range 0.24-24 kg/day was obtained according to a $[Fe(II)]_0$ value in the range 0.02-2 M, which was similar to data reported by other authors for the production of nanoAg particles using a SDR with a diameter of 19.5 cm [79].

4. Conclusions

This study reports about the optimization of metallic iron nanoparticles production by means of a lab-scale (disk diameter=8.5 cm) spinning disk reactor. The experiments conducted according to previously found optimal reagent concentrations and inlet flowrates allowed to select the optimal rotational velocity (1400 rpm) and optimal distance of injection feed points from the disk centre (3.5 cm). According to these optimal parameter's values, monodisperse metallic iron nanoparticles were produced, characterized by a mean size of 28 ± 2.1 nm. The experimental results were interpreted considering the hydrodynamic field established on the rotating disk surface, modelling the rotating thin liquid film with classical models. In particular, Nusselt model returned higher film thickness with respect to the predictions made by more complex models, such as Pigford and Lepehin-Riabchuk models, leading to erroneous considerations about the dispersed power energy on the rotating disk. It was found that, even for laminar flow regime and Ekman number larger than 2, the use of 2D and 3D models, such as Pigford and Lepehin-Riabchuk ones, was preferable in comparison to Nusselt one. In fact, the residence time estimation through the latter model was always 1 order of magnitude higher in comparison with those estimated by the former ones, leading to lower calculated ϵ values and possible errors in the experimental data interpretation.

References

- [1] J.A. Keelan, J.W. Leong, D. Ho, K.S. Iyer, Therapeutic and safety considerations of nanoparticle-mediated drug delivery in pregnancy, *Nanomedicine*. 10 (2015) 2229–2247. doi:10.2217/nnm.15.48.
- [2] S. Dev, P. Prabhakaran, L. Filgueira, K.S. Iyer, C.L. Raston, Microfluidic fabrication of cationic curcumin nanoparticles as an anti-cancer agent, *Nanoscale*. 4 (2012) 2575–2579. doi:10.1039/C2NR11502F.
- [3] Y.A. Goh, X. Chen, F.M. Yasin, P.K. Eggers, R.A. Boulos, X. Wang, H.T. Chua, C.L. Raston, Shear flow assisted decoration of carbon nano-onions with platinum nanoparticles, *Chem. Commun.* 49 (2013) 5171. doi:10.1039/c3cc41647j.
- [4] D. Ho, J. Zou, X. Chen, A. Munshi, N.M. Smith, V. Agarwal, S.I. Hodgetts, G.W. Plant, A.J. Bakker, A.R. Harvey, I. Luzinov, K.S. Iyer, Hierarchical Patterning of Multifunctional Conducting Polymer Nanoparticles as a Bionic Platform for Topographic Contact Guidance, *ACS Nano*. 9 (2015) 1767–1774. doi:10.1021/nn506607x.
- [5] Y. Zhu, Q. Wu, Synthesis of Magnetite Nanoparticles by Precipitation with Forced Mixing, *J. Nanoparticle Res.* 1 (1999) 393–396. doi:10.1023/A:1010091625981.
- [6] J.A. Giroto, R. Guardani, A.C.S.C. Teixeira, C.A.O. Nascimento, Study on the photo-Fenton degradation of polyvinyl alcohol in aqueous solution, *Chem. Eng. Process. Process Intensif.* 45 (2006) 523–532. doi:10.1016/j.cep.2005.12.001.
- [7] J.M. Ochando-Pulido, M. Stoller, L. Di Palma, A. Martinez-Ferez, Threshold performance of a spiral-wound reverse osmosis membrane in the treatment of olive mill effluents from two-phase and three-phase extraction processes, *Chem. Eng.*

- Process. Process Intensif. 83 (2014) 64–70. doi:10.1016/j.cep.2014.07.006.
- [8] A. Ochieng, M.S. Onyango, A. Kumar, K. Kiriamiti, P. Musonge, Mixing in a tank stirred by a Rushton turbine at a low clearance, Chem. Eng. Process. Process Intensif. 47 (2008) 842–851. doi:10.1016/J.CEP.2007.01.034.
- [9] Ž. Olujić, M. Jödecke, A. Shilkin, G. Schuch, B. Kaibel, Equipment improvement trends in distillation, Chem. Eng. Process. Process Intensif. 48 (2009) 1089–1104. doi:10.1016/J.CEP.2009.03.004.
- [10] M. Stoller, Technical optimization of a dual ultrafiltration and nanofiltration pilot plant in batch operation by means of the critical flux theory: A case study, Chem. Eng. Process. Process Intensif. 47 (2008) 1165–1170. doi:10.1016/j.cep.2007.07.012.
- [11] A. Deghles, U. Kurt, Treatment of tannery wastewater by a hybrid electrocoagulation/electrodialysis process, Chem. Eng. Process. Process Intensif. 104 (2016) 43–50. doi:10.1016/j.cep.2016.02.009.
- [12] S. Becht, R. Franke, A. Geißelmann, H. Hahn, An industrial view of process intensification, Chem. Eng. Process. Process Intensif. 48 (2009) 329–332.
- [13] A.S. Peshkovsky, S. Bystryak, Continuous-flow production of a pharmaceutical nanoemulsion by high-amplitude ultrasound: Process scale-up, Chem. Eng. Process. Process Intensif. 82 (2014) 132–136. doi:10.1016/j.cep.2014.05.007.
- [14] T.P. Vispute, H. Zhang, A. Sanna, R. Xiao, G.W. Huber, K.P. de Jong, Renewable chemical commodity feedstocks from integrated catalytic processing of pyrolysis oils., Sci. . 330 (2010) 1222–7. doi:10.1126/science.1194218.
- [15] G. Vilardi, M. Parisi, N. Verdone, Simultaneous aggregation and oxidation of nZVI in Rushton equipped agitated vessel: Experimental and modelling, Powder Technol. 353 (2019) 238–246. doi:10.1016/j.powtec.2019.05.033.

- [16] M. Stoller, J.M.O. Pulido, L. Di Palma, A.M. Ferez, Membrane process enhancement of 2-phase and 3-phase olive mill wastewater treatment plants by photocatalysis with magnetic-core titanium dioxide nanoparticles, *J. Ind. Eng. Chem.* 30 (2015) 147–152. doi:10.1016/j.jiec.2015.05.015.
- [17] L. Di Palma, D. Mancini, E. Petrucci, Experimental assessment of chromium mobilization from polluted soil by washing, *Chem. Eng. Trans.* 28 (2012) 145–150. doi:10.3303/CET1228025.
- [18] L. Di Palma, P. Ferrantelli, C. Merli, E. Petrucci, I. Pitzolu, Influence of Soil Organic Matter on Copper Extraction from Contaminated Soil, *Soil Sediment Contam.* 16 (2007) 323–335. doi:10.1080/15320380701285758.
- [19] L. Di Palma, Influence of indigenous and added iron on copper extraction from soil, *J. Hazard. Mater.* 170 (2009) 96–102. doi:10.1016/j.jhazmat.2009.04.128.
- [20] E. Petrucci, L. Di Palma, R. Lavecchia, A. Zuorro, Treatment of diazo dye Reactive Green 19 by anodic oxidation on a boron-doped diamond electrode, *J. Ind. Eng. Chem.* 26 (2015) 116–121. doi:10.1016/J.JIEC.2014.11.022.
- [21] E. Marsili, H. Beyenal, L. Di Palma, C. Merli, A. Dohnalkova, J.E. Amonette, Z. Lewandowski, Uranium removal by sulfate reducing biofilms in the presence of carbonates, *Water Sci. Technol.* 52 (2005) 49–55.
- [22] E. Marsili, H. Beyenal, L. Di Palma, C. Merli, A. Dohnalkova, J.E. Amonette, Z. Lewandowski, Uranium Immobilization by Sulfate-Reducing Biofilms Grown on Hematite, Dolomite, And Calcite, *Environ. Sci. Technol.* 41 (2007) 8349–8354. doi:10.1021/es071335k.
- [23] P. De Filippis, L. Di Palma, M. Scarsella, N. Verdone, Biological denitrification of high-nitrate wastewaters: A comparison between three electron donors, *Chem. Eng.*

- Trans. 32 (2013) 319–324.
- [24] L. Di Palma, C. Merli, M. Paris, E. Petrucci, A steady-state model for the evaluation of disk rotational speed influence on RBC kinetic: model presentation, *Bioresour. Technol.* 86 (2003) 193–200. doi:10.1016/S0960-8524(02)00137-2.
- [25] J. Ewel, C. Berish, B. Brown, N. Price, J. Raich, Slash and Burn Impacts on a Costa Rican Wet Forest Site, *Ecology*. 62 (1981) 816–829. doi:10.2307/1937748.
- [26] L. Di Palma, N. Verdone, The effect of disk rotational speed on oxygen transfer in rotating biological contactors, *Bioresour. Technol.* 100 (2009) 1467–1470. doi:10.1016/j.biortech.2008.07.058.
- [27] W. Wang, Y. Hua, S. Li, W. Yan, W. Zhang, Removal of Pb(II) and Zn(II) using lime and nanoscale zero-valent iron (nZVI): A comparative study, *Chem. Eng. J.* 304 (2016) 79–88. doi:10.1016/j.cej.2016.06.069.
- [28] L. Shi, Y.-M. Lin, X. Zhang, Z. Chen, Synthesis, characterization and kinetics of bentonite supported nZVI for the removal of Cr(VI) from aqueous solution, *Chem. Eng. J.* 171 (2011) 612–617. doi:10.1016/J.CEJ.2011.04.038.
- [29] S. Zha, Y. Cheng, Y. Gao, Z. Chen, M. Megharaj, R. Naidu, Nanoscale zero-valent iron as a catalyst for heterogeneous Fenton oxidation of amoxicillin, *Chem. Eng. J.* 255 (2014) 141–148. doi:10.1016/J.CEJ.2014.06.057.
- [30] H. Pullin, R. Springell, S. Parry, T. Scott, The effect of aqueous corrosion on the structure and reactivity of zero-valent iron nanoparticles, *Chem. Eng. J.* 308 (2017) 568–577. doi:10.1016/J.CEJ.2016.09.088.
- [31] L. Wang, J. Yang, Y. Li, J. Lv, J. Zou, Removal of chlorpheniramine in a nanoscale zero-valent iron induced heterogeneous Fenton system: Influencing factors and degradation intermediates, *Chem. Eng. J.* 284 (2016) 1058–1067.

- doi:10.1016/j.cej.2015.09.042.
- [32] C. Ahoba-Sam, K. Boodhoo, U. Olsbye, K.-J. Jens, Tailoring Cu Nanoparticle Catalyst for Methanol Synthesis Using the Spinning Disk Reactor, *Materials (Basel)*. 11 (2018) 154–165. doi:10.3390/ma11010154.
- [33] S. Mohammadi, A. Harvey, K.V.K. Boodhoo, Synthesis of TiO₂ nanoparticles in a spinning disc reactor, *Chem. Eng. J.* 258 (2014) 171–184.
doi:10.1016/J.CEJ.2014.07.042.
- [34] K.V.K. Boodhoo, R.J.J. Jachuck, Application of the Spinning-Disc Technology for Process Intensification in the Chemical Process Industry, in: *Process. by Centrifugation*, Springer US, 2001: pp. 7–17. doi:10.1007/978-1-4615-0687-4_2.
- [35] K. Boodhoo, A. Harvey, *Process intensification for green chemistry : engineering solutions for sustainable chemical processing*, John Wiley & Sons Inc, 2013.
- [36] S.F. Chin, K.S. Iyer, C.L. Raston, M. Saunders, Size Selective Synthesis of Superparamagnetic Nanoparticles in Thin Fluids under Continuous Flow Conditions, *Adv. Funct. Mater.* 18 (2008) 922–927. doi:10.1002/adfm.200701101.
- [37] L. Cafiero, G. Baffi, A. Chianese, R.J.J. Jachuck, Process Intensification: Precipitation of Barium Sulfate Using a Spinning Disk Reactor, *Ind. Eng. Chem. Res.* 41 (2002) 5240–5246. doi:10.1021/IE010654W.
- [38] K.V.K. Boodhoo, R.J. Jachuck, Process intensification: spinning disk reactor for styrene polymerisation, *Appl. Therm. Eng.* 20 (2000) 1127–1146. doi:10.1016/S1359-4311(99)00071-X.
- [39] S.D. Pask, O. Nuyken, Z. Cai, The spinning disk reactor: an example of a process intensification technology for polymers and particles, *Polym. Chem.* 3 (2012) 2698. doi:10.1039/c2py20237a.

- [40] D.J. Gunn, M.S. Murthy, Kinetics and mechanisms of precipitations, *Chem. Eng. Sci.* 27 (1972) 1293–1313. doi:10.1016/0009-2509(72)80105-2.
- [41] A. Mohammadi, K. Boodhoo, Online conductivity measurement of residence time distribution of thin film flow in the spinning disc reactor, *Chem. Eng. J.* 207–208 (2012) 885–894.
- [42] X. Feng, D.A. Patterson, M. Balaban, E.A.C. Emanuelsson, Characterization of liquid flow in the spinning cloth disc reactor: Residence time distribution, visual study and modeling, *Chem. Eng. J.* 235 (2014) 356–367. doi:10.1016/j.cej.2013.09.025.
- [43] G. Vilardi, M. Stoller, N. Verdone, L. Di Palma, Production of nano Zero Valent Iron particles by means of a spinning disk reactor, *Chem. Eng. Trans.* 57 (2017) 751–756. doi:10.1007/s00128-016-1865-9.
- [44] E. Gavi, D.L. Marchisio, A.A. Barresi, On the Importance of Mixing for the Production of Nanoparticles, *J. Dispers. Sci. Technol.* 29 (2008) 548–554. doi:10.1080/01932690701728965.
- [45] X. Chen, N.M. Smith, K.S. Iyer, C.L. Raston, Controlling nanomaterial synthesis, chemical reactions and self assembly in dynamic thin films, *Chem. Soc. Rev.* 43 (2014) 1387–1399. doi:10.1039/C3CS60247H.
- [46] M. Stoller, S. Vuppala, M. Matarangolo, V. Vaiano, D. Sannino, A. Chianese, C. Cianfrini, About a novel production method for N-doped magnetic nanocore nanoparticles of titania by means of a spinning disk reactor, 2017. doi:10.3303/CET1760008.
- [47] B. De Caprariis, M. Di Rita, M. Stoller, N. Verdone, A. Chianese, Reaction-precipitation by a spinning disc reactor: Influence of hydrodynamics on nanoparticles production, *Chem. Eng. Sci.* 76 (2012) 73–80. doi:10.1016/J.CES.2012.03.043.

- [48] G. Vilardi, N. Verdone, Production of metallic iron nanoparticles using Rushton and Four-Pitched Blade impellers in baffled stirred tank reactor: optimization and interpretation by computational fluid dynamics simulation, *Particuology*. Under Review (2019).
- [49] S. Li, Y. Ding, W. Wang, H. Lei, A facile method for determining the Fe(0) content and reactivity of zero valent iron, *Anal. Methods*. 8 (2016) 1239–1248.
doi:10.1039/C5AY02182K.
- [50] M. Stoller, L. Miranda, A. Chianese, Optimal feed location in a spinning disc reactor for the production of TiO₂ nanoparticles, *Chem. Eng. Trans.* 17 (2009) 993–998.
doi:10.3303/CET0917166.
- [51] I. V. Shevchuk, *Modelling of Convective Heat and Mass Transfer in Rotating Flows*, Springer International Publishing, London, 2016. doi:10.1007/978-3-319-20961-6.
- [52] O.K. Matar, C.J. Lawrence, G.M. Sisoiev, The flow of thin liquid films over spinning disks: Hydrodynamics and mass transfer, *Phys. Fluids*. 17 (2005).
doi:10.1063/1.1891814.
- [53] D.E. Hartley, W. Murgatroyd, Criteria for the break-up of thin liquid layers flowing isothermally over solid surfaces, *Int. J. Heat Mass Transf.* 7 (1964) 1003–1015.
doi:10.1016/0017-9310(64)90042-0.
- [54] K.V.K. Boodhoo, S.R. Al-Hengari, Micromixing Characteristics in a Small-Scale Spinning Disk Reactor, *Chem. Eng. Technol.* 35 (2012) 1229–1237.
doi:10.1002/ceat.201100695.
- [55] M.F. Majnis, N.Y. Azudin, S.R.A. Shukor, A.L. Ahmad, A Study on the Mixing Characteristics of Thin Liquid Film Flows over Horizontal Spinning Disk Surface, *Procedia Eng.* 148 (2016) 957–962. doi:10.1016/J.PROENG.2016.06.469.

- [56] R.M. Wood, B.E. Watts, The flow, heat and mass transfer characteristics of liquid films on rotating discs, *Chem. Eng. Res. Des.* 51a (1973) 315–322.
- [57] G. Leneweit, K.G. Roesner, R. Koehler, Surface instabilities of thin liquid film flow on a rotating disk, *Exp. Fluids*. 26 (1999) 75–85. doi:10.1007/s003480050266.
- [58] J.R. Burns, C. Ramshaw, R.J. Jachuck, Measurement of liquid film thickness and the determination of spin-up radius on a rotating disc using an electrical resistance technique, *Chem. Eng. Sci.* 58 (2003) 2245–2253. doi:10.1016/S0009-2509(03)00091-5.
- [59] G.I. Lepehin, G. V. Riabchuk, Temperature Distribution in Film of Viscous Liquid with Heating on a Rotating Disk, *Rheol. Process. Appar. Chem. Technol. Work. Polytech. Inst. Volgogr.* (1975) 82–91.
- [60] I. Leshev, G. Peev, Film flow on a horizontal rotating disk, *Chem. Eng. Process.* 42 (2003) 925–929. doi:10.1016/S0255-2701(02)00191-5.
- [61] N. Wakao, T. Funazkri, Effect of fluid dispersion coefficients on particle-to-fluid mass transfer coefficients in packed beds, *Chem. Eng. Sci.* 33 (1978) 1375–1384. doi:10.1016/0009-2509(78)85120-3.
- [62] A. Liu, W.-X. Zhang, Fine structural features of nanoscale zero-valent iron characterized by spherical aberration corrected scanning transmission electron microscopy (Cs-STEM), *Analyst*. 139 (2014) 4512–4518. doi:10.1039/c4an00679h.
- [63] C.R. Keenan, D.L. Sedlak, Factors Affecting the Yield of Oxidants from the Reaction of Nanoparticulate Zero-Valent Iron and Oxygen, *Environ. Sci. Technol.* 42 (2008) 1262–1267. doi:10.1021/es7025664.
- [64] X. Zhao, W. Liu, Z. Cai, B. Han, T. Qian, D. Zhao, An overview of preparation and applications of stabilized zero-valent iron nanoparticles for soil and groundwater

- remediation, *Water Res.* 100 (2016) 245–266. doi:10.1016/j.watres.2016.05.019.
- [65] R.A. Crane, T.B. Scott, Nanoscale zero-valent iron: Future prospects for an emerging water treatment technology, *J. Hazard. Mater.* 211–212 (2012) 112–125. doi:10.1016/J.JHAZMAT.2011.11.073.
- [66] X. Wang, L. Le, A. Wang, H. Liu, J. Ma, M. Li, Comparative study on properties, mechanisms of anionic dispersant modified nano zero-valent iron for removal of Cr(VI), *J. Taiwan Inst. Chem. Eng.* 66 (2016) 115–125. doi:10.1016/J.JTICE.2016.05.049.
- [67] F. Fu, D.D. Dionysiou, H. Liu, The use of zero-valent iron for groundwater remediation and wastewater treatment: A review, *J. Hazard. Mater.* 267 (2014) 194–205. doi:10.1016/j.jhazmat.2013.12.062.
- [68] S.H. Joo, A.J. Feitz, D.L. Sedlak, T.D. Waite, Quantification of the Oxidizing Capacity of Nanoparticulate Zero-Valent Iron, *Environ. Sci. Technol.* 39 (2004) 1263–1268. doi:10.1021/ES048983D.
- [69] J.T. Nurmi, P.G. Tratnyek, V. Sarathy, D.R. Baer, J.E. Amonette, K. Pecher, C. Wang, J.C. Linehan, D.W. Matson, R.L. Penn, M.D. Driessen, Characterization and properties of metallic iron nanoparticles: spectroscopy, electrochemistry, and kinetics., *Environ. Sci. Technol.* 39 (2005) 1221–30. doi:10.1021/es049190u.
- [70] G. Vilardi, D. Sebastiani, S. Miliziano, N. Verdone, L. Di Palma, Heterogeneous nZVI-induced Fenton oxidation process to enhance biodegradability of excavation by-products, *Chem. Eng. J.* 335 (2018) 309–320. doi:10.1016/j.cej.2017.10.152.
- [71] X. Li, W. Zhang, Iron Nanoparticles: the Core–Shell Structure and Unique Properties for Ni(II) Sequestration, *Langmuir.* 22 (2006) 4638–4642. doi:10.1021/LA060057K.
- [72] V. Schaller, U. Kräling, C. Rusu, K. Petersson, J. Wipenmyr, A. Krozer, G.

- Wahnström, A. Sanz-Velasco, P. Enoksson, C. Johansson, Motion of nanometer sized magnetic particles in a magnetic field gradient, *J. Appl. Phys.* 104 (2008) 913–918.
doi:10.1063/1.3009686.
- [73] J.K. Lim, S.P. Yeap, S.C. Low, Challenges associated to magnetic separation of nanomaterials at low field gradient, *Sep. Purif. Technol.* 123 (2014) 171–174.
doi:10.1016/j.seppur.2013.12.038.
- [74] S.P. Yeap, J. Lim, B.S. Ooi, A.L. Ahmad, Agglomeration, colloidal stability, and magnetic separation of magnetic nanoparticles: collective influences on environmental engineering applications, *J. Nanoparticle Res.* 19 (2017) 368–382.
doi:10.1007/s11051-017-4065-6.
- [75] S.P. Yeap, S.S. Leong, A.L. Ahmad, B.S. Ooi, J. Lim, On Size Fractionation of Iron Oxide Nanoclusters by Low Magnetic Field Gradient, *J. Phys. Chem. C.* 118 (2014) 24042–24054. doi:10.1021/jp504808v.
- [76] D. Ghiasy, M.T. Tham, K.V.K. Boodhoo, Control of a Spinning Disc Reactor: An Experimental Study, *Ind. Eng. Chem. Res.* 52 (2013) 16832–16841.
doi:10.1021/ie4020149.
- [77] J.R. Burns, R.J.J. Jachuck, Determination of liquid–solid mass transfer coefficients for a spinning disc reactor using a limiting current technique, *Int. J. Heat Mass Transf.* 48 (2005) 2540–2547. doi:10.1016/j.ijheatmasstransfer.2004.11.029.
- [78] B.K. Johnson, R.K. Prud'homme, Chemical processing and micromixing in confined impinging jets, *AIChE J.* 49 (2003) 2264–2282. doi:10.1002/aic.690490905.
- [79] C.Y. Tai, Y.-H. Wang, C.-T. Tai, H.-S. Liu, Preparation of Silver Nanoparticles Using a Spinning Disk Reactor in a Continuous Mode, *Ind. Eng. Chem. Res.* 48 (2009) 10104–10109. doi:10.1021/ie9005645.

Journal Pre-proof